





Dynamics of waste proteins in brain tissue: Numerical insights into Alzheimer’s risk factorsLily Watkins ¹, Saikat Mukherjee ^{1,2} and Jeffrey Tithof ^{1,*}¹*Department of Mechanical Engineering, University of Minnesota, Minneapolis, Minnesota 55455, USA*²*Department of Mechanical Engineering, Iowa State University, Ames, Iowa 50011, USA* (Received 6 October 2023; revised 31 May 2024; accepted 14 August 2024; published 3 September 2024)

Over the past few decades, research has indicated that the buildup of waste proteins, like amyloid- β ($A\beta$), in the brain’s interstitial spaces is linked to neurodegenerative diseases like Alzheimer’s, but the details of how such proteins are removed from the brain are not well understood. We have developed a numerical model to investigate the aggregation and clearance mechanisms of $A\beta$ in the interstitial spaces of the brain. The model describes the volume-averaged transport of $A\beta$ in a segment of the brain interstitium modeled as a porous medium, oriented between the perivascular space (fluid-filled channel surrounding a blood vessel) of a penetrating arteriole and that of a venule. Our numerical approach solves N coupled advection-diffusion-aggregation equations that model the production, aggregation, fragmentation, and clearance of N species of $A\beta$. We simulate $N = 50$ species to investigate the oligomer-size dependence of clearance and aggregation. We introduce a timescale plot that helps predict $A\beta$ buildup for different neurological conditions. We show that a sudden increase in monomer concentration, as occurs in conditions like traumatic brain injury, leads to significant plaque formation, which can qualitatively be predicted using the timescale plot. Our results also indicate that impaired protein clearance (as occurs with aging) and fragmentation are both mechanisms that sustain large intermediate oligomer concentrations. Our results provide novel insight into several known risk factors for Alzheimer’s disease and cognitive decline, and we introduce a unique framing of $A\beta$ dynamics as a competition between different timescales associated with production rates, aggregation rates, and clearance conditions.

DOI: [10.1103/PhysRevE.110.034401](https://doi.org/10.1103/PhysRevE.110.034401)**I. INTRODUCTION**

Alzheimer’s disease (AD) is a neurodegenerative disease and the most prevalent form of dementia in older adults. AD patients exhibit memory loss and overall cognitive decline, and recent pharmacological interventions have shown marginal therapeutic results [1]. In the United States alone, AD is the fifth leading cause of death in older populations, and the cost of care for AD patients exceeds \$300 billion annually [2]. There is a need for presymptomatic diagnoses as AD pathology is thought to begin at least 20 years before noticeable symptoms arise, at which point significant neuronal dysfunction and death have already occurred [2]. Since an effective cure for AD remains elusive, the number of AD patients is projected to double within the next 40 years [2]. Thus, there is a crucial need to understand the underlying causes of AD to develop effective prevention, diagnosis, and treatment strategies.

One of the key indicators in diagnosing AD is the presence of $A\beta$ plaques in the interstitial spaces of the brain [3]. The waste protein amyloid- β ($A\beta$) forms naturally in the brain as a monomer, which self-aggregates into larger assemblies called oligomers. As an oligomer becomes larger, it may eventually adopt a fibril morphology and become lodged in the brain tissue, at which point it is considered plaque. Note that we do not distinguish between oligomers of spherical versus fibrillar

morphology, and therefore we use the terms “oligomer” and “aggregate” interchangeably. $A\beta$ has been linked to several neurodegenerative diseases, including AD [3,4], but its exact role in AD is debated. There are two leading theories on the role of $A\beta$ in neurodegenerative diseases: the amyloid cascade hypothesis and the toxic oligomer hypothesis. In the amyloid cascade hypothesis, AD is believed to be caused by the large buildup of $A\beta$ plaque in the interstitial spaces [5,6]. Thus, patients with higher plaque concentrations are expected to have a more significant cognitive decline [6]. In contrast, the toxic oligomer hypothesis states that $A\beta$ oligomers are responsible for the cognitive decline associated with AD, which implies that a potential treatment or prevention of AD is tied to reducing $A\beta$ oligomer concentrations [7,8]. Cerebrospinal fluid (CSF) studies have shown elevated concentrations of oligomers of size 10–50 monomers as the distinguishing factor between control patients and AD patients; additionally, *in vivo* studies have shown higher neurotoxicity of oligomers relative to monomers [4]. Thus, oligomers of size 10–50 monomers are hypothesized to contribute to cognitive decline. The present study examines a few possible factors that can increase plaque accumulation and oligomeric concentrations.

The clearance of $A\beta$ from the brain has been estimated to be due to a combination of transport across the blood-brain barrier (25%), proteolytic degradation (50%), and interstitial fluid (ISF) drainage to the CSF (25%) [9]. In the present study, we focus on the last clearance mechanism, involving waste protein transport through the interstitial space to the perivascular spaces (PVSs), which are annular channels

*Contact author: tithof@umn.edu

surrounding the vasculature in the brain. Experimental reports of CSF transport along PVSs date back decades [10,11], but the importance of such transport for $A\beta$ clearance was only shown about a decade ago [12]. In 2012, Iliff *et al.* [12] demonstrated that $A\beta$ is actively cleared along PVSs and is dependent on astrocytes (a type of glial cell), which highly express a water channel protein, aquaporin-4; they dubbed this pathway the “glymphatic” (glial-lymphatic) system. Despite many important, subsequent discoveries from the past decade, many open questions remain regarding the details of the glymphatic system. We point the reader to a couple of recent review articles [13,14] for further information.

The dominant mechanism transporting $A\beta$ from the interstitial space to the PVS is debated [15]. Diffusion certainly plays a role, but the possibility of transport via bulk flow of interstitial fluid has been extensively debated [10,16–18]. Such flow is likely quite slow and has proven challenging to measure directly in experiments [19]. An innovative magnetic resonance imaging approach concluded that large solutes are transported by both advection and diffusion [20], and recent modeling studies have estimated parenchymal flow speeds in the range of about 2–5 $\mu\text{m}/\text{min}$ (close to the PVS) [21–24]. For relatively large molecules like $A\beta$, this implies that the Péclet number Pe (which characterizes the ratio of the diffusive transport timescale to the advective transport timescale) is likely not much larger than unity under physiological conditions. Bulk flow through PVSs, on the other hand, is likely much faster than that of interstitial flow and could conceivably sweep away $A\beta$ and similar solutes quickly enough to constitute an effective clearance mechanism [18].

In addition to open questions regarding the dominant modality of $A\beta$ transport, the causes of increased oligomeric concentrations and plaque deposition are poorly understood. However, evidence suggests that in most cases, $A\beta$ accumulation results from a clearance impairment rather than excess production [25]. Thus, in the present study, we use computational modeling to explore the mechanisms by which $A\beta$ accumulates. In particular, we examine the effects of initial concentrations, impaired clearance, advection, and fragmentation (the breakage of longer protein aggregates into smaller ones). Computational modeling offers the unique ability to vary each of these parameters and methodically test their effects on $A\beta$ kinetics in a way that cannot be precisely achieved in experiments.

Several models have been proposed to study the transport of $A\beta$ in the interstitial spaces of the brain by combining the discrete Smoluchowski aggregation equation with diffusion [26–28]. A model proposed by Knowles *et al.* [29] focuses on the aggregation and fragmentation of $A\beta$ through analytical solutions of a system of coupled nonlinear ordinary differential equations based on polymer nucleation to understand the oligomer size and time dependence of the coagulation processes. Schreck *et al.* [30] compared the analytical solution to the Smoluchowski aggregation equations by matching the overall mass of the aggregates to experimental data to show the validity of both methods. They found similarities between the models regarding aggregate mass but discrepancies in oligomer size distributions, leading to vastly different predictions between the models. Additionally, Schreck compared size-independent and size-dependent aggregation rates to

experimental fit. Ultimately, Schreck proposes size-dependent rates for aggregation of the Smoluchowski model, as this more closely matched experimental values [30], which we follow in the present study.

In our previous study [24], we proposed a three-species model of $A\beta$ aggregation and clearance from the interstitial space. The model uses Smoluchowski aggregation kinetics with size-dependent aggregation rates and includes monomer production. To study their relative importance, the model also couples advective and diffusive transport through the interstitial spaces. In this previous study, we showed an exponential decrease in accumulation for $Pe > 1$, as well as an increase in clearance due to the sleep-wake cycle [24]. However, our further development of the model revealed a few shortcomings. First, using three species does not allow the determination of oligomer size dependence on the various factors. It has also been shown that $A\beta$ aggregates exceed the aggregate of size three monomers [4]; thus a three-species model may not fully capture the complex aggregation and fragmentation dynamics. Additionally, the model did not consider the fragmentation of any species, which is a factor that is believed to sustain the concentrations of intermediate oligomeric species, which are potentially toxic [4]. Thus, in the present study, we aim to obtain novel—and more realistic—insights by extending our model to incorporate these factors.

This article is structured as follows. In Sec. II, we present our numerical approach by introducing the governing equations and parameters for our model, as well as the computational domain and timescales obtained from the nondimensionalization. We then present several results in Sec. III, including models of a healthy brain in Sec. III A, traumatic brain injury (involving a large release of $A\beta$ monomers) in Sec. III C, and the impact of impaired monomer clearance due to aging in Sec. III D. We then continue our study of aging with impaired clearance of all species in Sec. III E, introduce advection in Sec. III F, and finally investigate the effects of fragmentation in Sec. III G. Section IV provides the conclusions of our study.

II. APPROACH

A. Domain

$A\beta$ is produced naturally in the brain as a monomer, i.e., a single protein molecule. The monomers begin to aggregate and form larger assemblies called oligomers, which aggregate both with monomers and other oligomers. We model the aggregation process up to a cutoff size, at which point we consider the protein aggregate to be a plaque. In our previous study, we used a cutoff size of three monomers [24]. However, in the present study we consider an aggregate of 50 or more monomers to be the cutoff size for plaque formation. This choice follows the results of Hayden *et al.* [4], which showed increased neurotoxicity for oligomers of size 10–50 monomers. Additionally, a plaque aggregate of size 50 monomers may have a maximum length of up to about 12 nm [31] (depending on the arrangements of the protein molecules), which is comparable to the typical interstitial channel diameter [32] and can potentially become lodged in the interstitial space. In our model, a protein aggregate of size

i is essentially an aggregate of i monomers. Our model does not distinguish between linear fibrils and globular aggregates. We also tested homogeneous simulations (i.e., those with no diffusion, advection, or spatial extent) to vary the cutoff size for plaque formation, and we found the results to be independent of cutoff size, with final concentrations decreasing significantly for aggregates larger than 50 monomers. The plaques once formed do not contribute to the reaction except for Sec. III G; the plaques are allowed to fragment into smaller aggregates that become a site for the aggregation reaction. During the coagulation process, $A\beta$ can also fragment [30], although it is unknown if plaques can fragment, and we do not know the significance of this fragmentation. Thus, we expanded our previous model [24] to include the effects of fragmentation.

For our computational domain, we model a region in the brain in the vicinity of a penetrating arteriole and venule, as shown in Fig. 1(a). We assume that this domain is a portion of an infinite tiling of more arterioles and venules [22,24], and we apply corresponding (no flux) boundary conditions based on symmetry. Note that this domain is half of that in our prior study [24] and therefore more computationally efficient but perfectly equivalent due to symmetry. The computational domain consists of the brain interstitium located between a penetrating arteriole and venule [colored gray in Fig. 1(a)]. Figure 1(b) shows the complex, heterogeneous structure of the brain parenchyma, which is composed of neuronal and glial cells, capillaries, and the interstitial space [33]. The coagulation process is illustrated in Fig. 1(c), which shows the classification process of different species into monomers, oligomers, and plaques, as well as some of the aggregation and fragmentation pathways. In addition to coagulation, the proteins also move through the brain along PVSs, which are considered to be clearance pathways, as previously discussed. However, to reach a PVS, the proteins must move through the interstitial space shown in Fig. 1(b), by diffusion and potentially advection. In this paper, we model the protein transport to the PVSs through the interstitial spaces (which we model as a volume-averaged porous media) and the protein coagulation.

B. Smoluchowski coagulation kinetics

The aggregation and fragmentation of $A\beta$ proteins are modeled using Smoluchowski coagulation kinetics, which captures every combination of protein aggregate size concentrations c_r, c_s from monomers through plaques and prescribes size-dependent aggregation rates $a_{r,s}$ [27] and size-independent fragmentation rates b [30],

$$c_r + c_s \xrightleftharpoons[b]{a_{r,s}} c_{r+s}. \quad (1)$$

Here $1 \leq r \leq N$ and $1 \leq s \leq N$, where $N = 50$ is the number of species, and c_r and c_s are the concentration of protein aggregates of size r and s , respectively. Following the derivation presented by Schreck *et al.* [30], the scheme can be written as a summation of the aggregation and fragmentation of a particular combination of aggregate sizes r and s as a function of time by introducing a coagulation flux, $W_{r,s}(t)$,

$$W_{r,s}(t) = a_{r,s}c_r(t)c_s(t) - bc_{r+s}(t). \quad (2)$$

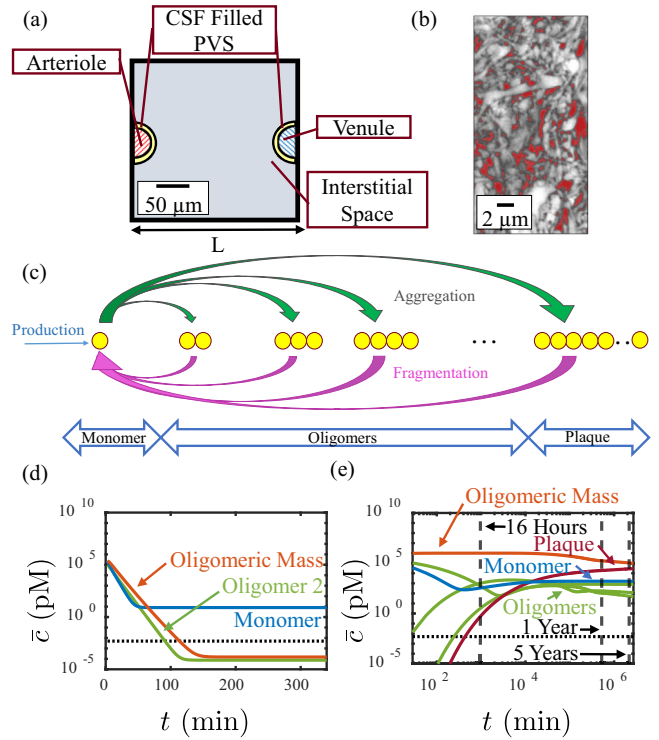


FIG. 1. Representation of the spatial domain and the coagulation scheme. (a) The 2D spatial domain used, composed of half an arteriole and half a venule surrounded by the PVSs. (b) Image of the interstitial space (red) obtained via super-resolution shadow imaging. (c) Schematic of the coagulation scheme, including aggregation, fragmentation, and monomer production. (d) The temporal variation of the spatially averaged concentration of protein species from a 2D diffusion simulation with complete clearance ($C_i = 0$), 1 μM monomer initial concentration, and no fragmentation (Sim. 1). The green lines represent Oligomer 2. (e) The temporal variation of the concentration of protein species from a homogeneous simulation with 1 μM monomer initial concentration and no fragmentation, with vertical lines showing various points in time. From highest concentration to lowest, the green lines represent the concentrations of Oligomers 2, 20, and 40. Concentrations below 5×10^{-3} pM [black dotted lines in (d) and (e)] are assumed to be governed by noncontinuum dynamics. Panel (b) adapted from Ref. [34] with permission.

The flux can then be summed over all species to yield the overall coagulation rate for a given species of size $i > 1$ as a function of time, $F_i(t)$ [30]:

$$F_i(t) = \frac{1}{2} \sum_{s=1}^{i-1} W_{s,i-s}(t) - \sum_{s=1}^N W_{i,s}(t). \quad (3)$$

The forcing function is applied to all species. Furthermore, the aggregation rate of two proteins, $a_{r,s}$, is a function of the protein aggregate size and the aggregation rate of two monomers, $a_{1,1}$:

$$a_{r,s} = \frac{a_{1,1}}{r \cdot s}. \quad (4)$$

The aggregation scheme is based on end-to-end aggregation proposed using statistical mechanics arguments by Tomski and Murphy [35] and later verified using *in vitro* coagulation

studies by Murphy and Pallito [36]. The aggregation scheme presented here is simplified based on the analysis from a prior modeling study by Bertsch *et al.* [27]. Note that the value of $a_{1,1}$ and other parameters are provided below in Sec. II G. The fragmentation rates were determined from experimental values and assumed to be independent of protein aggregate size [30].

C. Monomer production

To account for monomer production, a production term, f_p , is added to the forcing function for the monomers,

$$F_1(t) = \sum_{s=1}^N W_{1,s}(t) + f_p. \quad (5)$$

We assume that monomers are produced uniformly across the domain and that the production rate is independent of the monomer concentration. Our production term f_p should be interpreted as an “effective” production rate accounting for the limitation that our model only captures one $A\beta$ clearance mechanism. Our model does not include an intracellular compartment wherein substantial $A\beta$ clearance occurs via proteolytic degradation (e.g., via endothelin-converting enzyme-1 [37]) prior to secretion into the ECS. In addition, our model ignores blood-brain barrier efflux of extracellular $A\beta$. Since Roberts *et al.* [9] estimated that drainage of interstitial fluid (i.e., the clearance mechanism we model in this study) accounts for about 25% of total $A\beta$ removal, we use an effective production rate that is 25% of the estimated true total production rate.

D. Advection-diffusion

In addition to coagulation, $A\beta$ proteins can also move through the interstitial space due to ISF suspension. The movement is attributed to diffusion and possible advection, which is debated as previously discussed. In the first part of our results, we present simulations without advective transport, in which transport is purely diffusive. These simulations utilize the standard diffusion equation, which uses the effective diffusivity, D_{eff} , of the protein species in the interstitial space,

$$\frac{\partial c_i}{\partial t} = D_{\text{eff},i} \nabla^2 c_i. \quad (6)$$

The effective diffusivity of the protein species is modeled by using the tortuosity of the interstitial space, λ , and the diffusivity of $A\beta$ monomer in a free medium, D , and it is inversely proportional to the cube root of the molecular weight (in our study, a protein aggregate of size i is i times the molecular weight of $A\beta$ monomer), which assumes a compact globule [24],

$$D_{\text{eff},i} = \frac{D}{\lambda^2 \times i^{\frac{1}{3}}}. \quad (7)$$

In cases with nonzero advective transport, the velocity field is modeled via Darcy’s law (since we model the interstitium as a porous medium),

$$\vec{v} = -k \vec{\nabla} P, \quad (8)$$

where k is the hydraulic conductivity, P is the average pressure in the domain, and \vec{v} is the volume-averaged fluid velocity. The velocity field obtained is then applied to evolve the concentration field via advection and diffusion,

$$\frac{\partial c_i}{\partial t} = \vec{v} \cdot \vec{\nabla} c_i + D_{\text{eff},i} \nabla^2 c_i. \quad (9)$$

E. Governing equation

The coagulation and transport due to advection and diffusion are then combined and nondimensionalized to yield the governing equation for the time evolution of the concentration of each $A\beta$ species, c_i ,

$$\frac{\partial c_i}{\partial t} = \frac{1}{\text{Pe}_i} \nabla^2 c_i - \vec{v} \cdot \vec{\nabla} c_i + F_i. \quad (10)$$

We apply the governing equation to all protein species, $i \in [1, N]$. However, the plaques are considered immobile aggregates, which are unable to move out of the domain through diffusion or advection (i.e., $\frac{\partial c_N}{\partial t} = F_N$). A no-flux boundary condition is enforced along all walls. A Dirichlet boundary condition is also enforced along the PVSs. The governing equation is then solved in Fortran using a second-order accurate in space and first-order accurate in time finite-difference scheme. For complete clearance, zero concentration is enforced at the PVSs for all species. For impaired clearance, a nonzero concentration is enforced. Finally, to model completely impaired clearance, the spatial extent is removed from the governing equation, and only the coagulation term is used to evaluate the concentration evolution. We refer to the latter scenario as the “homogeneous” simulation.

In addition to the concentration of individual species, it is useful to also compute the overall oligomeric mass M of the system [30],

$$M = \sum_{i=2}^{N-1} i c_i, \quad (11)$$

which allows us to quantify the prevalence of intermediate oligomers.

F. Timescales

Once the governing equation is determined, it is nondimensionalized using a characteristic length (L), timescale (T_A), pressure scale (ΔP), and concentration scale (c_{scale}) [24]. The characteristic length of the system is taken to be the typical distance between a penetrating arteriole and venule in primates, $L = 250 \mu\text{m}$ [22,24]. Through nondimensionalization, we obtain several timescales associated with advection, diffusion, and coagulation, which characterize the relative strengths of each mechanism. The characteristic advection timescale, T_A , is a function of the length, the pressure difference across the domain ΔP , and hydraulic conductivity of the interstitial space, k ,

$$T_A = \frac{L^2}{\Delta P k}. \quad (12)$$

We use the advection timescale to nondimensionalize the other parameters. The diffusion timescale, T_D , is defined using

the effective diffusivity and the lengthscale, such that

$$T_D = \frac{L^2}{D_{\text{eff}}}. \quad (13)$$

The Péclet number, Pe , is defined as the ratio between the diffusion and advection timescales, and it can be used to vary the relative strength of diffusion to show the effects of advection versus diffusion,

$$Pe = \frac{T_D}{T_A}. \quad (14)$$

The production timescale, T_{f_p} , is defined using the characteristic concentration scale c_{scale} and production rate,

$$T_{f_p} = \frac{c_{\text{scale}}}{f_p}. \quad (15)$$

The aggregation timescale, $T_{a_{r,s}}$, is then determined using the concentration scale and aggregation rates,

$$T_{a_{r,s}} = \frac{1}{a_{r,s}c_{\text{scale}}}. \quad (16)$$

Finally, the fragmentation timescale, T_b , is defined using the fragmentation rate,

$$T_b = \frac{1}{b}. \quad (17)$$

By evaluating the timescales at varying concentrations, we can develop an intuition for the mechanisms that play a prominent role in the dynamics of $A\beta$ transport in different neurological disorders.

G. Parameters

Next, we note the values of the different parameters used in the simulations. The monomer production rate is taken as $f_p = 3.48 \times 10^{-14} \text{ M s}^{-1}$ [24], the monomer-to-monomer aggregation rate used is $a_{11} = 6.6 \times 10^3 \text{ M}^{-1} \text{ s}^{-1}$ [24], and the fragmentation rate used is $b = 1.8 \times 10^{-7} \text{ s}^{-1}$ [30]. The concentration scale is set to be equal to the initial monomer concentration in the domain. We used a diffusivity of $D = 2.3 \times 10^{-10} \text{ m}^2/\text{s}$ and a tortuosity of $\lambda = 2.04$ [22,24,38]. We also used $\Delta P = 0.275 \text{ mmHg}$ [24] for $Pe = 1$. The lengthscale was determined using the typical distance between a venule and arteriole in a primate brain of $L = 250 \text{ }\mu\text{m}$. The hydraulic conductivity used is $k = 200 \text{ }\mu\text{m}^2 \text{ mmHg}^{-1} \text{ s}^{-1}$ [22,24]. Additionally, unless otherwise stated, we start all simulations with zero initial concentration for all species other than the monomers.

H. Impaired clearance parameter

Due to the flow of CSF in the PVSs surrounding the interstitium, any $A\beta$ molecule of monomer or oligomer is potentially cleared out by that flow as soon as it reaches the PVS from the interstitium. For such a case, a Dirichlet boundary condition like $c_i = 0$ is a reasonable assumption. However, we explore the possibility that this boundary condition may change due to a neurological condition. The worst-case scenario is a full blockage of clearance at the PVS with a boundary condition of dimensionless concentration unity, similar to a homogeneous simulation devoid

of diffusion and advection. In that scenario, we expect that the steady-state concentration will not be achieved due to monomer production. Instead, the concentration of all species will continue to increase. Experiments indicate that periods of sleep drive more clearance in the brain than periods of wakefulness [39,40]; thus we focus on the worst potential buildup during a 16-h day in a diseased brain, i.e., running a 16-h homogeneous simulation that yields the concentration for each protein species. We then introduce an impaired clearance parameter, α , which is a fraction of this 16-h homogeneous concentration in the domain set at the PVSs. We are then able to model the boundary concentration for each protein species at the PVS, $c_{i,BC}$:

$$c_{i,BC} = \alpha c_{i,H16}. \quad (18)$$

In the equation, $c_{i,BC}$ is the concentration of a given aggregate of size i enforced as the boundary condition at the PVSs, and α is the impaired clearance parameter, which varies from 0 to 1. $c_{i,H16}$ is the homogeneous concentration of a given aggregate of size i after 16 h of fully impaired clearance.

I. Simulations

Each 2D simulation presented in this study is summarized in Table I.

III. RESULTS AND DISCUSSION

A. Limiting cases

We start by comparing two limiting cases for 2D simulations with purely diffusive transport (no advection): perfect clearance ($\alpha = 0$) at the boundaries and fully impaired clearance. In a model of fully impaired clearance, the proteins are not swept away at the PVS, so a concentration gradient does not form throughout the 2D domain; the concentration field is instead uniform and at a higher concentration relative to the 2D diffusive clearance case. Hence, there is no spatial dependence on the concentration, and the domain can be reduced to a single point in space. We refer to this fully impaired clearance scenario as the ‘‘homogeneous simulation.’’ Figures 1(d) and 1(e) compare the 2D diffusion scenario (d) to the homogeneous simulation (e), where both simulations start from identical $1 \text{ }\mu\text{M}$ monomer initial concentrations and do not include fragmentation. To determine the lower bound on the concentration that would represent a significant number of $A\beta$ molecules in the domain such that continuum approximation is valid, we consider the depth of the domain to be the typical length of a penetrating arteriole ($1000 \text{ }\mu\text{m}$) [41]. A single $A\beta$ monomer results in a concentration of $2.6 \times 10^{-5} \text{ pM}$. We consider 200 monomer molecules a significant concentration for continuum approximation, thus resulting in a lower concentration cutoff of $5 \times 10^{-3} \text{ pM}$ for all species. In some simulations, the concentrations dropped below this threshold, so we have added a black dotted line in the figures to represent concentrations below the continuum approximation in order to still provide intuition for general trends.

Figure 1(d) shows the results of Sim. 1, where it can be seen that the monomers and smaller aggregates maintain a small steady-state concentration, with the larger oligomers and plaque having concentrations that are negligible (below

TABLE I. Details of each 2D simulation presented in the study. Sims. 4–7 only have nonzero boundary conditions for the monomers.

Sim no.	IC c_1	IC c_i ($2 \leq i \leq 49$)	IC c_{50}	BC	Pe	Fragmentation?	Fig. no.
1	1 μ M	0	0	0	0	NO	1,3,4
2	1 pM	0	0	0	0	NO	3
3	10^8 pM	0	0	0	0	NO	3
4	1 μ M	0	0	1 pM (c_1)	0	NO	4
5	1 μ M	0	0	10 pM (c_1)	0	NO	4
6	1 μ M	0	0	100 pM (c_1)	0	NO	4
7	1 μ M	0	0	1000 pM (c_1)	0	NO	4
8	1 μ M	$c_{i,H16}$	$c_{i,H16}$	$\alpha = 0$	0	NO	5,6
9	1 μ M	$c_{i,H16}$	$c_{i,H16}$	$\alpha = 0.0001$	0	NO	5,6
10	1 μ M	$c_{i,H16}$	$c_{i,H16}$	$\alpha = 0.001$	0	NO	5,6
11	1 μ M	$c_{i,H16}$	$c_{i,H16}$	$\alpha = 0.01$	0	NO	5,6
12	1 μ M	$c_{i,H16}$	$c_{i,H16}$	$\alpha = 0.1$	0	NO	5,6
13	1 μ M	$c_{i,H16}$	$c_{i,H16}$	$\alpha = 0.5$	0	NO	5,6
14	1 μ M	$c_{i,H16}$	$c_{i,H16}$	$\alpha = 0$	3	NO	6
15	1 μ M	$c_{i,H16}$	$c_{i,H16}$	$\alpha = 0.0001$	3	NO	6
16	1 μ M	$c_{i,H16}$	$c_{i,H16}$	$\alpha = 0.001$	3	NO	6
17	1 μ M	$c_{i,H16}$	$c_{i,H16}$	$\alpha = 0.01$	3	NO	6
18	1 μ M	$c_{i,H16}$	$c_{i,H16}$	$\alpha = 0.1$	3	NO	6
19	1 μ M	$c_{i,H16}$	$c_{i,H16}$	$\alpha = 0.5$	3	NO	6
20	1 μ M	$c_{i,H16}$	$c_{i,H16}$	$\alpha = 0$	10	NO	6
21	1 μ M	$c_{i,H16}$	$c_{i,H16}$	$\alpha = 0.0001$	10	NO	6
22	1 μ M	$c_{i,H16}$	$c_{i,H16}$	$\alpha = 0.001$	10	NO	6
23	1 μ M	$c_{i,H16}$	$c_{i,H16}$	$\alpha = 0.01$	10	NO	6
24	1 μ M	$c_{i,H16}$	$c_{i,H16}$	$\alpha = 0.1$	10	NO	6
25	1 μ M	$c_{i,H16}$	$c_{i,H16}$	$\alpha = 0.5$	10	NO	6
26	1 μ M	0	50 μ M	0	0	NO	7
27	1 μ M	0	50 μ M	0	0	YES	7

a cutoff of 5×10^{-3} pM). However, in the homogeneous simulation for which diffusive clearance is not present [Fig. 1(e)], the concentrations of all proteins increase substantially. The homogeneous simulations show the effect of aggregation and monomer production. A recent study involving a three-species Smoluchowski model (with monomer production) [42] reported that the first two species achieve steady-state concentrations after about 500 days, implying that from that point on, all monomer production is immediately converted to the largest aggregate (analogous to plaque). We therefore expected to potentially see low/moderate steady-state concentrations for the oligomeric species and long-term increase in the concentration of only c_{50} . However, we instead see an increasing concentration of all oligomeric species for the five years of simulation. This seemingly unbounded increase in concentrations of all species lends credence to the toxic oligomer hypothesis and demonstrates how it may result from impaired clearance.

Thus, the most general diffusion scenario maintains low plaque and oligomeric concentrations and moderately higher monomer concentrations, whereas the fully impaired clearance scenario results in large concentrations of all species. These two simulations suggest that diffusive clearance can maintain low concentrations of monomers and all heavier species if clearance at the PVS is rapid enough that the $c_i = 0$ boundary condition is reasonable. However, when clearance is fully impaired (as in the homogeneous

simulation), concentrations of all species are several orders of magnitude higher and exhibit years-long transients.

B. Timescale plot

We generated the timescale plot shown in Fig. 2 by plotting the various timescales presented in Sec. II F against the concentration scale, $c_{\text{scale}} = \bar{c}_1 (t = 0)$. It is useful to note that when comparing the monomer production timescale and the diffusive clearance timescale, we have used a characteristic lengthscale of $L/2$, as this better represents the characteristic length for diffusion between a venule and arteriole in our domain. Even though the full 50-species model given by Eq. (10) is nonequilibrium because of the constant production of monomers (c_1) and the lack of clearance of plaques (c_{50}), the individual protein species can reach a steady-state concentration when the production and the clearance timescales match, as shown by the timescale plot.

C. Modeling traumatic brain injury with a large monomer initial condition

We next study the effect of a rapid release of monomers in the case of pure diffusion (no advection). Following a traumatic brain injury (TBI), both rapid plaque formation [43] and an overall increase in $A\beta$ concentration [44] have been observed; however, the exact mechanism and cause of this increase is not well understood. One hypothesis is that

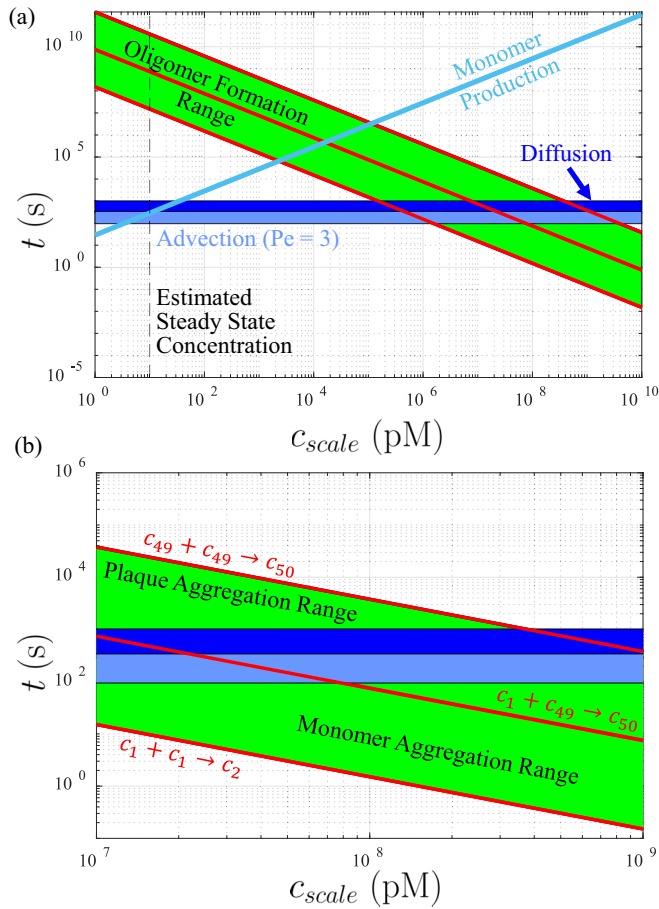


FIG. 2. (a) Timescale plot quantifying the relative importance of each transport mechanism as a function of the concentration scale. The timescales associated with oligomer aggregation are plotted as a band (green) where the red lines separate the monomer aggregation (lower) and plaque formation (upper) timescale regimes. The advection (light blue) and diffusion (dark blue) timescales are shown as horizontal lines. The monomer production timescale is also shown in teal. The vertical black dashed line represents the steady-state concentration predicted when the monomer production rate matches the diffusive clearance rate. (b) Zoomed-in version of (a) showing the slowest plaque formation timescale from oligomers ($c_{49} + c_{49} \rightarrow c_{50}$; top red line), the slowest monomer aggregation timescale or equivalently the fastest plaque formation timescale ($c_1 + c_{49} \rightarrow c_{50}$; middle red line), and the fastest monomer aggregation timescale ($c_1 + c_1 \rightarrow c_2$; bottom red line).

axon damage causes a rapid release of $A\beta$ that then leads to plaque formation [43]. A second hypothesis, which is not mutually exclusive with the first, suggests that TBI reduces glymphatic transport leading to impaired clearance of $A\beta$ from the interstitial space [45]. Regardless of the cause, elevated $A\beta$ concentrations are sustained for an extended time after the injury. To mimic this transient increase due to either hypothesized scenario, we start our simulations with a large monomer initial concentration.

We performed three simulations with purely diffusive transport, in which the monomer initial concentration was varied from 1 to 10^8 pM. These simulations (Sims. 1–3 in Table I) used the 2D domain without fragmentation and

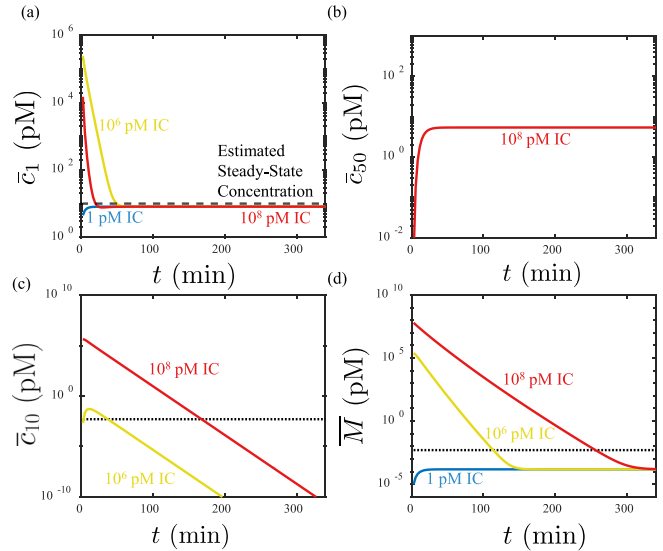


FIG. 3. TBI model that varies the monomer initial concentration from 1 to 10^8 pM (Sims. 1–3). (a) Effect of varying the monomer initial concentration on the spatially averaged monomer concentration, with the estimated steady-state monomer concentration represented as a black dashed line. (b) Effect of varying the monomer initial concentration on the plaque formation. (c) Effect of varying the monomer initial concentration on the spatially averaged concentration of Oligomer 20. (d) Effect of varying the monomer initial concentration on the spatially averaged concentration of the oligomeric mass. Concentrations below 5×10^{-3} pM [black dotted lines in (c) and (d)] are assumed to be negligible.

perfect clearance at the PVSs for all species ($\alpha = 0$). Before presenting the results, we first explain the aspects that can be inferred based on timescale arguments.

As seen in the timescale plot (Fig. 2), the intersection of the monomer production timescale and the diffusive clearance timescale leads to a prediction that a steady-state concentration is achieved at about 10 pM. We expect the monomer concentrations to asymptotically approach this value regardless of the starting concentration. In Fig. 3(a), the results of the simulations show that the monomers indeed approached the predicted steady-state concentration, with a value of 8.1 pM for all simulations, comparable to the 10 pM prediction. This shows that a sudden increase in monomer concentration will not change the long-term monomer steady-state concentration (under our assumptions of perfect clearance at the PVS).

In contrast, varying the monomer initial concentration results in substantial plaque (c_{50}) formation for a large monomer initial concentration. As seen in Fig. 3(b), a monomer initial concentration of 10^8 pM leads to a nonzero plaque formation, while the lower concentrations do not, where concentrations fall below 5×10^{-3} pM. This can also be predicted from the timescale plot in Fig. 2, where a value of monomer initial concentration larger than about 10^7 pM leads to faster plaque and oligomer formation than diffusion (i.e., beyond about 10^7 pM, the middle red line is lower than the dark blue band in Fig. 2). Indeed, the fastest plaque formation timescale due to a monomer and an oligomer of size 49 (middle red line) is faster than the diffusion timescale in the 10^8 pM scenario,

which triggers plaque formation. For the smaller monomer initial conditions, the diffusion timescale is several orders of magnitude faster than the plaque aggregation timescale, which results in negligible plaque formation. In contrast, for a monomer initial condition higher than about 10^7 pM, the plaque aggregation timescales are comparable to or faster than the diffusion timescale, leading to substantial plaque formation. Thus, it can be concluded that a large ($\gtrsim 10^7$ pM) initial bolus of monomers will lead to substantial plaque buildup, whereas a small ($\lesssim 10^6$ pM) initial monomer bolus will have minimal to zero plaque formation.

Next, we examine the effects of a large monomer initial concentration on the time series of oligomeric concentrations. Again, for larger concentrations (i.e., further right on the timescale plot, Fig. 2) we expect a shorter timescale over which aggregation occurs. In particular, above about 2×10^6 pM, the monomer aggregation (red diagonal line) and oligomer production (green diagonal band) become slightly faster than the diffusive clearance (dark blue horizontal band). Hence, for a given oligomer species, we expect a larger transient concentration when a larger monomer initial condition is used. However, these large transients should asymptotically approach much smaller values for three reasons: (i) they are no longer sustained by monomer aggregation as the monomer concentration returns to the steady-state value (about 10 pM), (ii) they are consumed to form heavier oligomers eventually aggregating into immobile plaque, and (iii) the oligomers are cleared out at the $\alpha = 0$ PVS boundary. Figure 3(c) shows the spatially averaged concentration of Oligomer 20 as a function of time, which confirms these predictions. The larger monomer initial concentration simulations show a significant increase in the concentration of Oligomer 20. However, as time progresses, the concentration drops rapidly, indicating the oligomer is no longer sustained by aggregation of lighter species and that it is being cleared to the PVSs and/or aggregating into plaque.

The oligomeric mass $[\bar{M}]$, see Eq. (11)] is plotted in Fig. 3(d) and confirms that the aforementioned trends hold for all oligomeric species. Specifically, we see that regardless of the monomer initial concentration, all simulations approach a common oligomeric mass steady-state concentration at longer times. This steady-state concentration is dictated primarily by the steady-state concentration values of smaller aggregates such as c_2 , as the concentration of larger aggregates is minimal. As explained before, large monomer initial concentrations lead to transient peak concentrations of intermediate oligomers, which are then depleted in long times due to a combination of reduced production (due to decreased monomer concentration), diffusive clearance at the PVS, and plaque formation.

D. Modeling aging: Impaired monomer clearance at the PVSs

We next explore the effect of impaired monomer clearance at the PVSs. Experiments on mice have shown that overall glymphatic flow and solute transport significantly decline with age [46–48]. Kress *et al.* showed a 40% reduction in A β clearance in aged mice [47]. Ma *et al.* showed a reduction in CSF drainage to lymphatic vessels in aged mice, indicative of reduced brain waste clearance [48]. Additionally, Kress

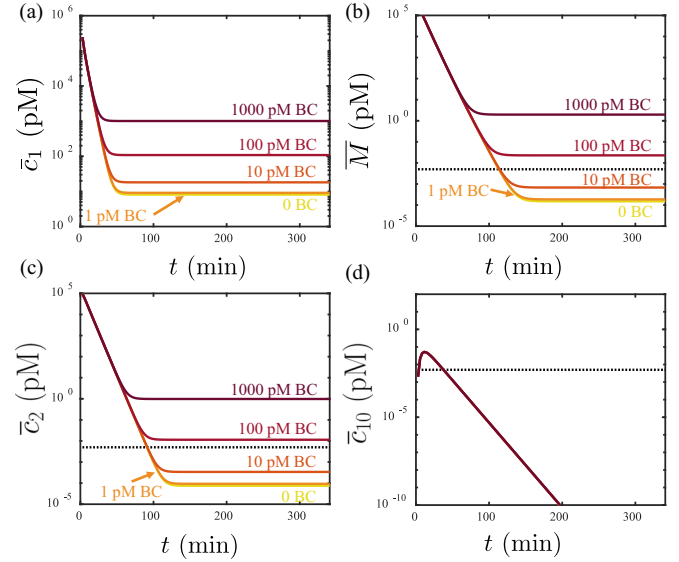


FIG. 4. Effects of impaired monomer clearance investigated by varying the monomer boundary condition (BC) at the PVSs from 0 to 1000 pM, with a 1 μ M monomer initial concentration (Sims. 1, 4–7 in Table I). The color gradient corresponds to the level of impaired clearance, with darker color representing greater impairment (i.e., higher concentration at the PVS boundary, as labeled). (a)–(d) Effect on the spatially averaged (a) monomer, (b) oligomeric mass, (c) Oligomer 2, and (d) Oligomer 20 concentrations over time. In panel (d), all of the simulations resulted in nearly identical, overlapping results, which appear as a single line. Concentrations below 5×10^{-3} pM [black dotted lines in (b), (c), and (d)] are assumed to be negligible.

et al. proposed that reduced clearance contributes to the cognitive decline associated with aging [47]. Reduced clearance increases the likelihood of A β plaque formation [46]. Studies measuring A β levels in ISF found that A β concentrations were age-dependent, with higher concentrations found in older mice [49].

In the present study, we model the effects of reduced glymphatic clearance with aging by varying the boundary conditions at the PVSs for the monomers while enforcing perfect clearance ($\alpha = 0$) for the oligomers. Since the PVSs are CSF-filled spaces, impaired clearance implies the CSF in the PVSs is not swept away as rapidly, and therefore it may contain some non-negligible level of A β proteins. Thus, we can model impaired clearance by enforcing a constant nonzero concentration of A β at the PVS. We begin by only enforcing a nonzero PVS boundary condition for the monomers, but further below we consider nonzero boundary conditions for all species (see Sec. III E). For each simulation presented here, we started with a 10^6 pM monomer initial concentration and no fragmentation. We then conducted separate simulations in which the boundary concentration at the PVSs for only the monomers varied from 0 to 1000 pM (Sims. 1, 4–7 in Table I).

The simulations show an overall increase in concentrations for smaller aggregates as the monomer concentration at the PVS boundary increases. Figure 4(a) shows the spatially averaged concentration of monomers \bar{c}_1 as a function of time. For the monomers, we see an approximately linear relation-

ship between the boundary concentration and steady-state concentration for boundary concentrations ≥ 10 pM, implying impaired clearance has a large effect on the monomer steady-state concentration. Similar results are seen for the oligomeric mass in Fig. 4(b), with an approximately linear relation for boundary concentrations above 10 pM. As the impairment in monomer clearance increases, the oligomeric mass steady-state concentration also increases. As before, most of the oligomeric mass concentration is attributed to the smaller aggregates, as observed through comparison of Figs. 4(c) and 4(d), which show the concentrations of Oligomers 2 and 20, respectively. In Fig. 4(c), the concentration of Oligomer 2 is relatively large, and the steady-state concentration increases with the monomer boundary concentration. In Fig. 4(d), the concentration of Oligomer 20 is small and continually decreases until it drops below a negligible value of 5×10^{-3} pM at about 300 min. Overall, monomer clearance impairment leads to an increase in smaller oligomers, whereas larger oligomers remain virtually unaffected [e.g., Fig. 4(d)]. We note that for all cases plaque concentrations were negligible, thus they are not shown in Fig. 4.

E. Modeling aging: Impaired monomer and oligomer clearance at the PVSs

Realistically, we would expect reduced CSF flow through PVSs to increase the PVS boundary concentration of not only the monomers but also the oligomers. Thus, we further explore the effect of impaired clearance at the PVSs by examining the consequences of nonzero PVS boundary conditions applied to all species. We quantify the impact of impaired clearance by testing different values of the impaired clearance parameter ($0 \leq \alpha < 1$). As previously described, α specifies the concentration at the PVS boundary as a fraction of the concentration of a given species from the 16-h homogeneous simulation. The homogeneous simulation represents a worst-case scenario in which clearance is absent and the monomers are only produced and aggregate into oligomers and plaque. Hence, the concentrations reached after 16h in the homogeneous simulation represent the maximum possible concentration of each species gained during the day (when glymphatic clearance is least active). The level of impaired clearance can then be varied from zero ($\alpha = 0$) to the 16-h homogeneous simulation concentrations ($\alpha = 1$). Each simulation we present next (Sims. 8–13) was started from a $1 \mu\text{M}$ initial monomer concentration. The initial concentration of all oligomeric species and plaque was set to corresponding values from the 16-h homogeneous simulation at $\alpha = 1$ throughout the entire interior of the domain [see the interstitial space in Fig. 1(a)]. The PVS boundary concentration was maintained according to the impaired clearance condition given by Eq. (18), where α was varied from 0 to 0.5, with 0 representing perfect PVS clearance.

Figure 5(a) shows the concentration of the oligomeric mass (M) across the domain at three instances in time: initial conditions, transient, and steady-state conditions. Transient is defined as the time at which 98% of the asymptotic solute clearance has occurred. The upper panels show M for $\alpha = 0.01$ while the lower panels show M for $\alpha = 0$.

Figure 5(a) shows that when $\alpha = 0.01$, the boundary condition determines the concentration in the domain at steady state, while when $\alpha = 0$ at the PVS, the steady-state concentration is determined by the competition between diffusive clearance and production (as shown in Sec. III A).

At the start of each simulation, the initial concentration for species 1–49 in the domain's interior is set to the 16-h homogeneous concentration. As time increases, diffusion transports the monomers and oligomers to the PVSs. When the PVS boundary clearance is substantially impaired (i.e., $\alpha \gtrsim 0.1$), the diffusive clearance reduces the concentration inside the domain until it matches the concentration maintained at the boundary, as shown in the upper rightmost panel in Fig. 5(a). In this scenario, at steady state, oligomers continue to form through aggregation but are immediately either cleared out or aggregate into plaques. In contrast, for the case with $\alpha = 0$ [bottom panel in Fig. 5(a)], the overall concentrations are much lower (maximum concentration of oligomeric mass in the domain is around 2×10^{-4} pM), and a gradient is maintained in the domain for the entirety of the simulation (although the lower rightmost panel in Fig. 5 does not show this gradient due to the color bar's scaling). The gradient has a maximum concentration of 1.6×10^{-4} (pM) and a minimum concentration of zero at the PVSs. The gradient occurs because when $\alpha = 0$ at the PVS, the steady-state concentration is determined by the competition between diffusive clearance and monomer production (which can be predicted based on matching the timescales, $T_D = T_{f_p}$).

The effect of impaired clearance on the monomers is shown in Fig. 5(b). We see that as α increases, the steady-state concentration increases. We can also calculate a predicted steady-state concentration for the monomers by applying Eq. (18) to the monomer final concentration. In Fig. 5(b), it is seen that the predicted concentrations match well with the steady-state concentrations obtained from the simulations for $\alpha \gtrsim 0.1$. However, when $\alpha \lesssim 0.1$, Eq. (18) yields values of monomer concentrations that are less than the steady-state concentration of monomers when $\alpha = 0$ at the PVS in our simulations. This is because monomer clearance in our simulation domain is diffusion-limited. When $\alpha = 0$ at the PVS, regardless of the initial condition, the monomer steady-state concentration ($\bar{c}_1 = 8.1$ pM) is set by the competition between diffusive clearance and monomer production rates ($T_D = T_{f_p}$), whereas in homogeneous simulations, lowering the initial condition leads to lower values of monomer steady-state concentration.

Figure 5(c) shows the spatially averaged steady-state values of select species as a function of α . Overall, the concentration of all the protein species increases monotonically with α . For the plaques (red circular data points), changing α has little effect on the final concentrations until $\alpha \approx 0.5$, where the final concentration increases. The plaque concentrations do not reach a steady state, but rather slowly increase. In contrast, the intermediate oligomers (green circular data points) increase linearly with α . A deviation from the linear behavior is observed in the monomers for $\alpha < 0.01$, wherein they reach a steady-state value that becomes independent of α as α continues to decrease. This steady-state concentration is again due to the diffusion-limited nature of monomer transport at lower values of α , where the steady-state concentration

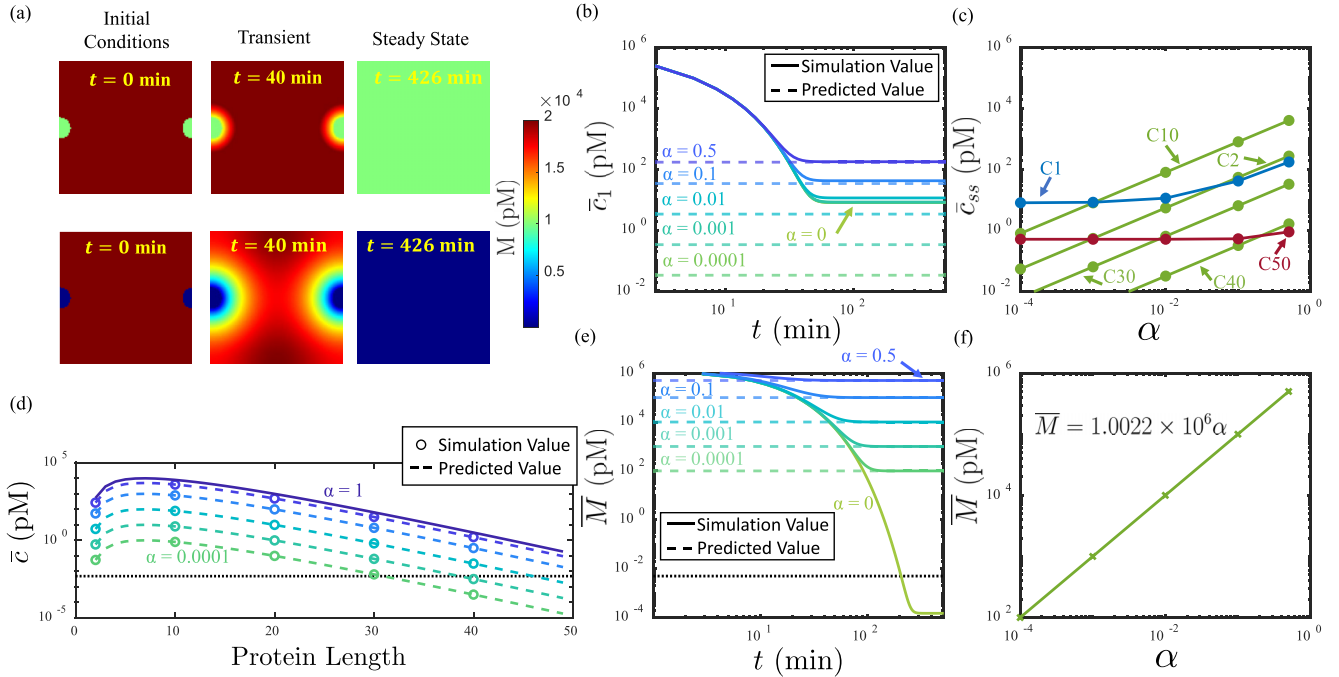


FIG. 5. Effect of varying the impaired clearance parameter α from 0 to 0.5 (Sims. 8–13). (a) The oligomeric mass concentration field for $\alpha = 0.01$ (upper panels) vs $\alpha = 0$ (lower panels) at three time instances: the initial condition, time to clear 98% of the solute that will be cleared asymptotically, and the time to reach steady state. A small gradient is present in the lower right panel that is not discernible. Note that the maximum concentrations in the far left panels are much higher than the upper limit of the color map. (b) Spatially averaged monomer concentration as a function of time for various values of α ; both the simulation results (solid) and the predicted value (dashed) are plotted. (c) Steady-state values for select species as a function of α . Plaque concentrations (c_{50}) are slowly increasing, so values shown are the final values of the simulation rather than a steady-state concentration. (d) The final concentrations of oligomers from simulations (circles) and values predicted by the impaired clearance parameter (dashed lines). (e) Spatially averaged oligomeric mass concentration for different values of α with both the simulation results (solid) and predicted value based on Eq. (19) (dashed). (f) Steady-state oligomeric mass concentration for different values of α showing a line of best fit of $\bar{M} = 1.0022 \times 10^6 \alpha$ (pM). Concentrations below 5×10^{-3} pM [black dotted lines in (d) and (e)] are assumed to be negligible.

is determined by the competition of diffusive transport and monomer production.

Since the boundary conditions determine the interior concentrations for each oligomer species (at least for the values of α tested), we can predict the concentration we expect each oligomer to reach using Eq. (18). We then further calculate a predicted oligomeric mass steady-state concentration using the concentration enforced at the boundary by combining the impaired clearance parameter [Eq. (18)] with the oligomeric mass [Eq. (11)]:

$$\bar{M}_{\text{predicted}} = \sum_{i=2}^{49} i c_{H16} \alpha = \bar{M}_{H16} \alpha. \quad (19)$$

Figure 5(d) shows the final oligomer concentrations of the 16-h homogeneous simulation as a function of the aggregate size in the solid line. The figure also shows the expected steady-state concentrations (dashed lines) generated based on the homogeneous simulation results via Eq. (19) and the simulated steady-state values (circles) for each α . The agreement between the two is excellent.

Figure 5(d) also indicates that aggregates of size 2–20 are at higher concentrations than longer proteins. This suggests that our choice of $N = 50$ is adequate for resolving the dynamics of the formation of larger oligomers and

plaques. Previous experimental studies have confirmed that the amyloid- β size distribution is dominated by species of smaller size [50,51]. It is interesting to note that the aggregation rate of larger size oligomers is inversely proportional to their size, which can contribute to the size distribution observed. Homogeneous simulations lead to substantial concentrations of intermediate oligomers (c_2 to c_{40}), as is evident from Fig. 5(d). Furthermore, we see higher concentrations of smaller oligomers, which is reflected in Fig. 5(c), where Oligomers 2 and 10 had higher steady-state concentrations than Oligomers 30 and 40 (for fixed α). We also observe in Fig. 5(d) that the highest oligomer concentrations are for sizes 5–10, again seen in Fig. 5(c) through Oligomer 10 having a higher concentration than Oligomer 2.

We next compare the predicted oligomeric mass concentrations to the spatially averaged oligomeric mass from the simulations, as shown in Fig. 5(e). As α increases, the steady-state value of the oligomeric mass also increases, and for the nonzero α values considered, the steady-state values of the oligomeric mass agree well with the predicted values. Figure 5(f) shows the steady-state value of the spatially averaged oligomeric mass concentration (from the simulation) as a function of α . A line of best fit applied to the plot shows that the oligomeric mass and α are linearly related through $\bar{M} = 1.0022 \times 10^6 \alpha$ (pM). This linear relationship matches what

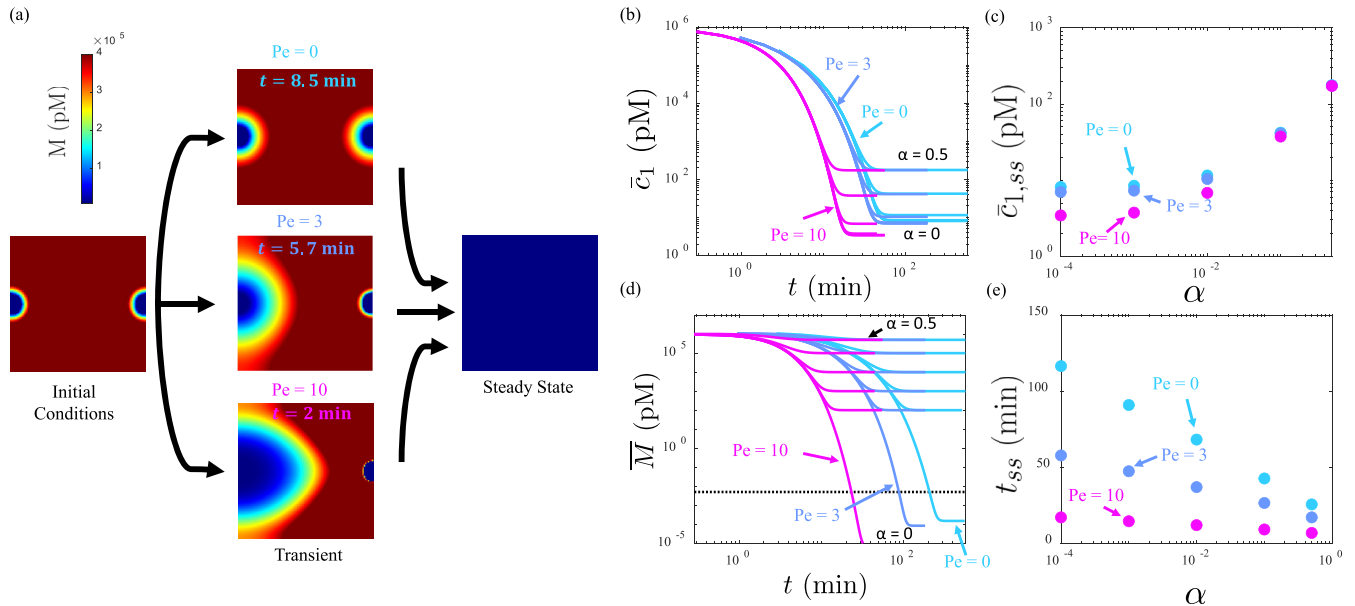


FIG. 6. Effects of advective vs diffusive clearance on impaired clearance ($\alpha = [0, 0.0001, 0.001, 0.01, 0.1, 0.5]$), where pure diffusion corresponds to $Pe = 0$ (Sims. 8–25). (a) Spatial distribution of oligomeric mass for each value of Pe at the initial condition, at 50% of the total solute clearance, and at steady state; the initial and final distributions were identical in all $\alpha \neq 0$ scenarios. (b) Spatially averaged monomer concentrations as a function of time. (c) The spatially averaged monomer concentration at steady state for each value of Pe as a function of the impaired clearance parameter, α . (d) Spatially averaged oligomeric mass concentration as a function of time for each scenario. (e) Time to steady state for the spatially averaged oligomeric mass concentration for each value of Pe as a function of α . Concentrations below 5×10^{-3} pM [black dotted line in (d)] are assumed to be negligible.

was observed using Eq. (19), which predicts that $\bar{M}_{\text{predicted}} = 1.0016 \times 10^6 \alpha$ (pM), using the 16-h homogeneous concentrations obtained with a $1 \mu\text{M}$ monomer initial concentration. Thus, the oligomeric mass follows the predicted trends.

F. Effects of advection

We continue the study of impaired clearance by investigating effects due to advection. As previously mentioned, the significance of advective clearance is debated. Since the diffusion coefficient decreases with increasing molecular weight, advective transport is expected to become increasingly important for large molecules [17]. Thus, we would expect to see advective clearance play a more significant role for heavier weight species (e.g., longer oligomers). To investigate the significance of advection on $A\beta$ transport, we vary the Péclet number Pe , which characterizes the relative strength of advection and diffusion. We tested three values of Pe : 0 (Sims. 8–13), 3 (Sims. 14–19), and 10 (Sims. 20–25). $Pe = 0$ is the pure diffusion case, which has been studied in Sec. III E. Although $Pe = 10$ is not expected under physiological conditions, we use this upper limit to clearly distinguish between diffusion-dominated and advection-dominated clearance. It is interesting to note that previous numerical studies have estimated an upper bound on the Péclet number to be about $Pe = 4$ [22].

For each simulation set, we also varied the impaired clearance parameter α from 0 to 0.5 to compare with the results presented in Sec. III E. As before, we started with the concentration of each species in the interior of the domain set to the full 16-h homogeneous concentration and the monomers

at a $1 \mu\text{M}$ initial concentration. The results of the advection simulations are plotted in Fig. 6.

Figure 6(a) shows the concentration field of the oligomeric mass for each value of Pe at the initial condition, 50% of solute clearance, and at steady state. For the pure diffusion scenario of $Pe = 0$, the clearance is symmetric about the vertical centerline. However, for the $Pe > 0$ cases, the clearance becomes asymmetric, with stronger advective clearance having a more pronounced effect on the concentration gradient across the domain. The pressure gradient is oriented across the domain such that the venule acts as a sink and the arteriole as a source. Thus, the flow is driven from the arteriole toward the venule. At larger Pe , the concentration around the arteriole decreases, because advection moves the proteins toward the venule. However, the concentration adjacent to the venule increases, and the gradient becomes steeper because both advection and diffusion are cotransporting solute toward the low concentration boundary at the venule. Correspondingly, the proteins will then pile up around the venule, as observed in the middle panels (labeled “Transient”), and gradually be cleared out. Ultimately, each case converged to the same steady state, as dictated by the impaired clearance parameter, α , as shown in the right panel (labeled “steady state”).

The spatially averaged monomer concentration for each value of Pe is shown in Fig. 6(b). For moderate advection strength ($Pe = 3$), the trends resemble the diffusive clearance scenario ($Pe = 0$); for both cases, increasing α leads to greater steady-state concentrations. We also observe that stronger advection decreases the time to steady state, as the monomers reach steady state significantly faster in the $Pe = 3$ versus $Pe = 0$ case. For the highest advection strength ($Pe = 10$),

the time to steady state is further reduced. Additionally for the $Pe = 10$ scenario, the steady-state concentration only reaches the predicted PVS concentration for a high impaired clearance parameter ($\alpha \geq 0.1$), as advection overpowers the monomer production rate, whereas the diffusion and weaker advection scenario reached or exceeded the predicted steady-state concentration for $\alpha \geq 0.01$. Thus, a high advective strength will reduce the time to steady state for the monomers as well as reduce steady-state concentration given little impaired clearance. In the timescale plot (Fig. 2), we see that advection (for $Pe = 3$) results in a timescale slightly shorter than that of diffusive clearance. Thus the time to steady state being reduced for the $Pe = 3$ and 10 simulations in Fig. 6(b) aligns with the expectations from the timescale plot.

The spatially averaged monomer steady-state concentration as a function of the impaired clearance parameter α is presented in Fig. 6(c). For small levels of impaired clearance, the steady-state concentrations vary significantly between the purely diffusive and strongly advective scenarios. However, as the impaired clearance increases, the concentrations converge to similar values for all three Pe . Thus, for little to no clearance impairment (i.e., small α), advection will further reduce the steady-state concentrations, but when clearance impairment is large, the only effect of advection is to reduce the time to reach steady state. Additionally, the $Pe = 0$ and 3 scenarios exhibit a nonlinear relationship between the monomer steady-state concentration and α at low impaired clearance ($\alpha \lesssim 0.01$); for $Pe = 10$, this relationship becomes nonlinear for $\alpha \lesssim 0.001$.

As shown in Fig. 6(d), the spatially averaged steady-state concentration for the oligomeric mass is identical for all three Pe cases when $\alpha \geq 0.0001$. However, for perfect clearance ($\alpha = 0$), the steady-state concentration decreases as the strength of advection increases. Additionally, the time to steady state also decreases as the advective strength increases. Since advection is movement due to bulk flow, and increasing the strength of advection effectively increases flow speed, a reduction in time to steady state is expected. Since the concentration in the domain is dictated by the concentration enforced at the PVS, this implies that monomers/oligomers in the interior of the domain will be cleared to the boundaries faster. The timescale plot presented in Sec. III B further illustrates the effect of advection on time to steady state. As observed in Fig. 2, the advection timescale for $Pe = 3$ is below the diffusive clearance timescale. Thus, we expect the proteins to reach a steady state faster when advection is present. The line of best fit was also determined for the steady-state concentration of the oligomeric mass as a function of the impaired clearance parameter α . For $Pe = 3$, $\bar{M} = 1.0017 \times 10^6 \alpha$ (pM) and for $Pe = 10$, $\bar{M} = 1.0016 \times 10^6 \alpha$ (pM). We find these equations to be comparable to the previously presented diffusion scenario of $\bar{M} = 1.0022 \times 10^6 \alpha$ (pM), further confirming that advection has minimal effects on the steady-state concentration for impaired clearance.

The time to steady state (t_{ss}) for the spatially averaged oligomeric mass as a function of the impaired clearance parameter α is shown in Fig. 6(e). As no overshoot was observed in any of the scenarios, the time to steady state was defined as the time for the simulation to clear 99% of the solute that will asymptotically be cleared. In Fig. 6(e), for small α values, the purely diffusive simulations had the longest time to steady

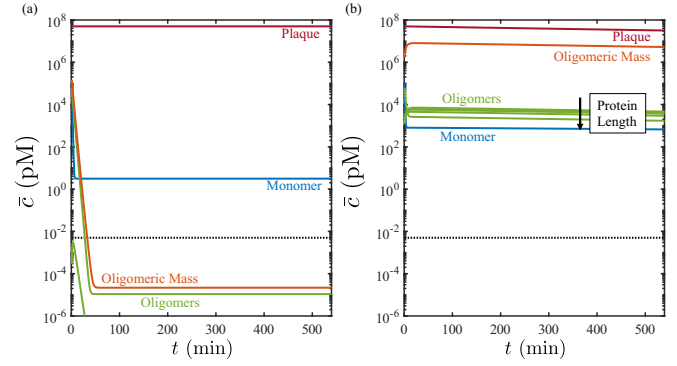


FIG. 7. Effect of fragmentation of all species for a $1 \mu\text{M}$ monomer initial concentration and a $50 \mu\text{M}$ plaque initial concentration in the purely diffusive model (Sims. 26–27). (a), (b) Spatially averaged concentration over time for (a) the no-fragmentation simulation and (b) the simulation with fragmentation of all species (excluding monomers). Concentrations below 5×10^{-3} pM [black dotted lines in (a) and (b)] are assumed to be negligible.

state, and t_{ss} in the advection cases decreased as the advective strength increased. However, as the impaired clearance level increased, t_{ss} for each scenario began to converge. Thus, the effects of advection on time to steady state are more prominent at lower levels of clearance impairment (i.e., lower α).

G. Effects of fragmentation

Finally, we study the effects of fragmentation on $A\beta$ clearance. Fragmentation is defined as the breakup of larger aggregates into smaller ones. Both numerical and analytical models of *in vitro* studies of $A\beta$ formation and self-assembly indicate the existence of $A\beta$ fragmentation [29,30]. However, the importance of $A\beta$ fragmentation on $A\beta$ clearance is relatively unknown. Specifically, the fragmentation of plaques may provide a mechanism for plaque clearance since plaques are immobile (i.e., not cleared by diffusion or advection); fragmentation may also help sustain concentrations of intermediate oligomers [52]. Fragmentation thus may be significant in AD and other neurodegenerative diseases where we expect the presence of plaques and larger aggregates in the brain. To explore the effect of fragmentation, we consider purely diffusive transport (Sims. 26–27) starting from a $1 \mu\text{M}$ monomer initial concentration. We also use the size-independent fragmentation rates proposed by Schreck *et al.* [30]. We begin with a large plaque initial concentration of $50 \mu\text{M}$, adapted from experimentally measured plaque levels in mice brains with AD [53].

We first establish the steady-state concentrations for simulations with no fragmentation, as shown in Fig. 7(a). The monomers quickly reach a low steady-state concentration of about 3 pM, which is smaller than the 8 pM concentration achieved when plaque initial concentration was zero (Fig. 3). The change can be attributed to the coagulation kinetics, which relies intricately on the initial concentration of each species. The oligomeric mass reaches a small steady-state concentration of 2×10^{-5} pM, which is mainly attributed to the smaller oligomers, as seen through Oligomer 2 having a nearly identical concentration profile to the oligomeric mass.

The plaque concentration remains constant [the change is less than 10^{-4} pM, Fig. 3(b)] for the duration of the simulation because the monomer production rate is small.

We next show the effect of oligomeric and plaque fragmentation in Fig. 7(b). In this case, the monomers reach a relatively high steady-state concentration of 790 pM. The oligomers also achieve high steady-state concentrations, with the oligomeric mass having relatively equal contributions from every species. Finally, the plaque concentration decreases slightly over time, which can be attributed to the fragmentation kinetics. In this scenario, the plaques fragment and feed the monomers and oligomers, increasing their concentrations but decreasing the overall plaque concentration. Therefore, fragmentation acts as a mechanism to remove plaque.

The effect of fragmentation can be obtained by comparing Figs. 7(a) and 7(b). We see that the monomer steady-state concentration increases by two orders of magnitude when fragmentation is present. This implies that monomers are forming from the fragmentation of longer proteins at a large rate, leading to an overall increase in monomer concentration, and diffusion is not fast enough to clear out these monomers. From the perspective of timescales (Fig. 2), fragmentation provides a new source of monomers that shifts the steady-state concentration between monomer production and diffusion to the right. The shift shortens the timescale for aggregation, which allows the monomer production to contribute more significantly to the formation of oligomers and plaque rather than being immediately cleared from the domain. For the oligomers, we see that fragmentation leads to large steady-state concentrations for all oligomeric species, whereas the no-fragmentation scenario leads to a small steady-state concentration only for short oligomers (and negligible concentration for longer oligomers); compare Figs. 7(a) and 7(b). Correspondingly, fragmentation leads to a large increase in oligomeric mass. This new steady-state concentration for oligomeric species is also reached significantly faster in the fragmentation case than the nonfragmentation case, as predicted by timescale arguments (Fig. 2). Finally, the plaque concentration decreases when fragmentation is present, which implies that fragmentation may be a mechanism to reduce plaque buildup.

IV. CONCLUSION

We have presented a numerical model of the aggregation and clearance of $A\beta$ protein species in the interstitial space. We investigated the effects of varying several key parameters that model salient aspects of different neurological disorders, including monomer initial condition as a model of TBI, and increasing $A\beta$ concentration at PVS boundaries as a model of aging. We also explored the role that hypothesized phenomena may play, including interstitial advection and oligomer/plaque fragmentation.

We first studied the sudden release of $A\beta$ monomers attributed to TBI and found little effect on $A\beta$ monomer and oligomeric steady-state concentrations, but a significant increase in plaque formation for a high (10^8 pM) monomer release (Fig. 1). Our results agree with clinical observations that show changes in plaque concentrations [43] rather than

long-term effects on monomer and oligomer concentrations. We expect that the drastic increase in plaque, if the monomer release is significant enough, will align with the rapid plaque formation seen in TBI patients [43]. A significant result of our TBI study is the ability to predict the steady-state monomer concentrations as well as understanding the strength of each mechanism using the timescale plot, which allows us to think of neurodegenerative diseases as a competition of timescales. The timescale approach can then be expanded to study other neurodegenerative diseases beyond TBI. Furthermore, we can use the timescale plot as a method for comparing specific clearance methods in the absence of a computational model that isolates those clearance methods.

Given the decline in glymphatic flow and/or CSF turnover observed in old age and AD patients [46–48], we then showed that impaired monomer clearance at the PVSs leads to an increase in monomer and smaller oligomer steady-state concentrations, but it has little impact on longer oligomer steady-state concentrations and plaque formation. Interestingly, for all simulations, the *rate* of approach to the steady-state value does not change significantly with α for any aggregate size, as seen in Figs. 4(b) and 4(e), where the curves are overlapping until the steady state is achieved. Rather, only the steady-state concentration changes when monomer clearance is impaired. The monomer-impaired clearance study implies that as the monomer concentration becomes non-negligible in the PVSs, attributed to aging, we expect an increase of $A\beta$ monomers and short oligomers in the interstitial spaces. However, we would not expect a drastic change in the concentrations of plaque and longer oligomers. This implies that the plaque buildup observed in AD patients is not necessarily due to impaired monomer clearance (at least under the assumptions here, including an absence of fragmentation).

However, when we allowed impaired clearance of all species, we saw an increase in steady-state concentrations of all oligomers. We predicted the steady-state concentrations of the oligomeric species and the oligomeric mass for different values of the impaired clearance parameter, α . For $0.0001 \leq \alpha \leq 0.5$, we found a linear relationship between α and the steady-state oligomeric mass concentration. From these simulations, we conclude that impaired clearance at the PVSs has a large impact on the presence of intermediate oligomers. Since plaque has no clearance mechanism in this scenario, its concentration must remain the same or increase. Given that the oligomeric steady-state concentrations all increase, we expect that impaired clearance of all species is a mechanism that will increase the rate of plaque formation. However, longer simulations are needed to determine asymptotic rates of plaque formation.

The magnitude and significance of advection in the brain's interstitium is debated in the literature [10,15–18,20–23]. From the advection-diffusion impaired clearance simulations, we provide insight into the role and significance of advection on $A\beta$ clearance. For impaired clearance ($0.0001 \leq \alpha \leq 0.5$), the steady-state concentrations remain unchanged for the oligomers; for the monomers, there is a slight reduction when α is low and Pe is large. For perfect clearance ($\alpha = 0$), advection reduces the oligomeric and monomer steady-state concentrations. In all scenarios, advection reduced the time to steady state for the monomers and oligomers. We also

observed that the presence of advection will break the reflection symmetry along the vertical centerline and will result in higher protein concentrations adjacent to the venule. Ultimately, our model of impaired clearance ($\alpha > 0$) is meant to capture a scenario in which flow of “clean” CSF through PVSs is not rapid enough to dilute the PVS $A\beta$ concentration to negligible levels. Our model suggests that impaired clearance (i.e., substantial PVS $A\beta$ concentrations) has a higher impact on oligomer steady-state concentrations and plaque formation than the presence of advection through the interstitium.

Finally, we studied the effect of fragmentation, which led to an increase in concentrations of both monomers and oligomers. This result is in agreement with experimental studies of protein aggregation [52] that demonstrate that fragmentation leads to larger concentrations of all species. In particular, plaque fragmentation helps sustain large steady-state concentrations of $A\beta$ oligomers. Intriguingly, when fragmentation occurs, the monomer steady-state concentration is increased, which shifts the characteristic timescales into a regime (i.e., to the right in Fig. 2) where a greater proportion of the monomers aggregate into oligomers and plaques rather than being cleared at the PVSs. Overall, we find that fragmentation reduced the amount of plaque present, implying that fragmentation is a mechanism for sustaining concentrations of potentially neurotoxic oligomers, and it may be a plaque clearance mechanism. These results frame plaque fragmentation as a potential mechanism to target when developing AD treatments, as reducing plaque fragmentation may reduce oligomeric concentrations.

Our model has many important limitations due to several simplifying assumptions. First, we only consider a 2D domain that analyzes the transport of $A\beta$ to the PVSs, and we ignore the details of $A\beta$ transport along the PVSs. Additionally, our model simplifies some aspects of $A\beta$ coagulation. While our model does include fragmentation, it does not include primary nucleation or surface catalyzed secondary nucleation. Previous modeling studies have included primary nucleation but have demonstrated that aggregation dynamics are dominated by secondary nucleation events [29,30]. In the future, we can add primary nucleation to our model. Recent experiments have further indicated the possibility that aggregation rates are size-independent, which will be updated in our model in the future [54]. We also assume size-independent fragmentation rates. While size-dependent fragmentation rates more closely fit experimental data [30], our results capture the qualitative effects of fragmentation, but future models could be extended to incorporate size-dependent fragmentation rates. Additionally, we ignore other clearance mechanisms such as direct blood-brain-barrier efflux, which can be included in

future studies. We also model the impaired clearance boundary conditions as a Dirichlet boundary condition with a constant value, which may not reflect the true PVS concentration variation. For fully impaired clearance, a no-flux boundary condition may be a better choice. A more realistic representation of the boundaries would involve modeling solute transport through the PVSs. Our model uses a rigid domain that assumes no tissue deformation or arterial pulsation; recent studies suggest that deformation of the brain parenchyma may be a critical aspect of the mechanics of glymphatic CSF transport [39,55,56]. We also assumed an idealized geometry for the venule and arteriole for our domain, which could be improved by using more realistic anatomy [57]. Finally, the interstitial space contains capillaries that also contribute to protein clearance via blood-brain barrier efflux, which could be incorporated in future models.

We will continue the development of our model to more precisely capture the complex dynamics of $A\beta$ clearance. We plan to characterize the effect of varying monomer production, aggregation rates, and size-dependent versus size independent fragmentation rates, as there is some disagreement in the literature regarding the true values [30,42]. Additionally, our model assumes the interstitial space is a uniform porous medium, so we may seek to increase the geometrical complexity to more accurately model the interstitial space [58]. Our future studies will also examine the impacts of the sleep-wake cycle, which involves running simulations for days rather than hours. Previous research has shown that sleep leads to an expansion of the interstitial space [40], which increases the permeability of the brain tissue, potentially making it more amenable to advective clearance. This effect can be included in our model by changing the Péclet number over the sleep-wake cycle. Finally, recent studies indicate CSF flow alterations in the PVSs due to spreading depolarization waves during stroke, migraine, and cardiac arrest [59–62]. Exploring how such alterations in CSF flow may affect the long-term dynamics of protein buildup in the brain interstitium would provide novel insights. This can be examined by combining a model of CSF flow in the PVSs [62] with the present model of interstitial transport.

ACKNOWLEDGMENTS

This work is supported by a Career Award at the Scientific Interface from Burroughs Wellcome Fund and the College of Science and Engineering at the University of Minnesota. The authors acknowledge the Minnesota Supercomputing Institute (MSI) at the University of Minnesota for providing resources that contributed to the results presented.

- [1] N. S. L. Yeo-Teh and B. L. Tang, *Sci. Eng. Ethics* **29**, 2 (2023).
- [2] Alzheimer’s Association, *Alzheimer’s Dement.* **20**, 3708 (2024).
- [3] M. Korsak and T. Kozyreva, in *Intrinsically Disordered Proteins Studied by NMR Spectroscopy*, edited by I. C. Felli and R. Pierattelli (Springer, Cham, Switzerland, 2015), pp. 401–421.
- [4] E. Y. Hayden and D. B. Teplow, *Alzheimers Res. Ther.* **5**, 60 (2013).

- [5] A. D. Korczyn, *Alzheimers Dement.* **4**, 176 (2008).
- [6] J. Hardy and D. J. Selkoe, *Science* **297**, 353 (2002).
- [7] H. Fukumoto, T. Tokuda, T. Kasai, N. Ishigami, H. Hidaka, M. Kondo, D. Allsop, and M. Nakagawa, *FASEB J.* **24**, 2716 (2010).
- [8] S. Oddo, A. Caccamo, L. Tran, M. Lambert, C. G. Glabe, W. L. Klein, and F. M. LaFerla, *J. Biol. Chem.* **281**, 1599 (2006).

- [9] K. F. Roberts, D. L. Elbert, T. P. Kasten, B. W. Patterson, W. C. Sigurdson, R. E. Connors, V. Ovod, L. Y. Munsell, K. G. Mawuenyega, M. M. Miller-Thomas *et al.*, *Ann. Neurol.* **76**, 837 (2014).
- [10] M. L. Rennels, T. F. Gregory, O. R. Blaumanis, K. Fujimoto, and P. A. Grady, *Brain Res.* **326**, 47 (1985).
- [11] T. Ichimura, P. Fraser, and H. F. Cserr, *Brain Res.* **545**, 103 (1991).
- [12] J. J. Iliff, M. Wang, Y. Liao, B. A. Plogg, W. Peng, G. A. Gundersen, H. Benveniste, G. E. Vates, R. Deane, S. A. Goldman *et al.*, *Sci. Transl. Med.* **4**, 147ra111 (2012).
- [13] D. H. Kelley and J. H. Thomas, *Annu. Rev. Fluid Mech.* **55**, 237 (2023).
- [14] T. Bohr, P. G. Hjorth, S. C. Holst, S. Hrabětová, V. Kiviniemi, T. Lilius, I. Lundgaard, K.-A. Mardal, E. A. Martens, Y. Mori, U. V. Nägerl, C. Nicholson, A. Tannenbaum, J. H. Thomas, J. Tithof, H. Benveniste, J. J. Iliff, D. H. Kelley, and M. Nedergaard, *iScience* **25**, 104987 (2022).
- [15] H. Mestre, Y. Mori, and M. Nedergaard, *Trends Neurosci.* **43**, 458 (2020).
- [16] B.-J. Jin, A. J. Smith, and A. S. Verkman, *J. Gen. Physiol.* **148**, 489 (2016).
- [17] J. Iliff and M. Simon, *J. Physiol.* **597**, 4417 (2019).
- [18] J. H. Thomas, *J. R. Soc. Interface* **16**, 20190572 (2019).
- [19] H. Mestre, J. Tithof, T. Du, W. Song, W. Peng, A. M. Sweeney, G. Olveda, J. H. Thomas, M. Nedergaard, and D. H. Kelley, *Nat. Commun.* **9**, 4878 (2018).
- [20] S. Koundal, R. Elkin, S. Nadeem, Y. Xue, S. Constantinou, S. Sanggaard, X. Liu, B. Monte, F. Xu, W. Van Nostrand *et al.*, *Sci. Rep.* **10**, 1990 (2020).
- [21] K. E. Holter, B. Kehlet, A. Devor, T. J. Sejnowski, A. M. Dale, S. W. Omholt, O. P. Ottersen, E. A. Nagelhus, K.-A. Mardal, and K. H. Pettersen, *Proc. Natl. Acad. Sci. USA* **114**, 9894 (2017).
- [22] L. Ray, J. J. Iliff, and J. J. Heys, *Fluids Barriers CNS* **16**, 1 (2019).
- [23] J. Tithof, K. A. S. Boster, P. A. R. Bork, M. Nedergaard, J. H. Thomas, and D. H. Kelley, *iScience* **25**, 104258 (2022).
- [24] S. Mukherjee and J. Tithof, *Phys. Rev. E* **105**, 024405 (2022).
- [25] K. R. Wildsmith, M. Holley, J. C. Savage, R. Skerrett, and G. E. Landreth, *Alzheimers Res. Ther.* **5**, 33 (2013).
- [26] Y. Achdou, B. Franchi, N. Marcello, and M. C. Tesi, *J. Math. Biol.* **67**, 1369 (2013).
- [27] M. Bertsch, B. Franchi, N. Marcello, M. C. Tesi, and A. Tosin, *Math. Med. Biol.* **34**, 193 (2017).
- [28] C. Y. Chen, Y. H. Tseng, and J. P. Ward, *Math. Biosci.* **317**, 108258 (2019).
- [29] T. P. J. Knowles, C. A. Waudby, G. L. Devlin, S. I. A. Cohen, A. Aguzzi, M. Vendruscolo, E. M. Terentjev, M. E. Welland, and C. M. Dobson, *Science* **326**, 1533 (2009).
- [30] J. S. Schreck and J. Yuan, *J. Phys. Chem. B* **117**, 6574 (2013).
- [31] A. E. Langkilde, K. L. Morris, L. C. Serpell, D. I. Svergun, and B. Vestergaard, *Acta Crystallogr. D* **71**, 882 (2015).
- [32] C. Nicholson and S. Hrabětová, *Biophys. J.* **113**, 2133 (2017).
- [33] C. Nicholson, *Rep. Prog. Phys.* **64**, 815 (2001).
- [34] J. Tønnesen, V. K. Inavalli, and U. V. Nägerl, *Cell* **172**, 1108 (2018).
- [35] S. J. Tomski and R. M. Murphy, *Arch. Biochem. Biophys.* **294**, 630 (1992).
- [36] R. M. Murphy and M. M. Pallitto, *J. Struct. Biol.* **130**, 109 (2000).
- [37] E. A. Eckman, M. Watson, L. Marlow, K. Sambamurti, and C. B. Eckman, *J. Biol. Chem.* **278**, 2081 (2003).
- [38] D. L. Adams, V. Piserchia, J. R. Economides, and J. C. Horton, *Cereb. Cortex* **25**, 3673 (2015).
- [39] L. Bojarskaite, A. Vallet, D. Bjørnstad, K. Gullestad Binder, C. Cunen, K. Heuser, M. Kuchta, K. Mardal, and R. Enger, *Nat. Commun.* **14**, 953 (2023).
- [40] L. Xie, H. Kang, Q. Xu, M. J. Chen, Y. Liao, M. Thiyagarajan, J. O'Donnell, D. J. Christensen, C. Nicholson, J. J. Iliff *et al.*, *Science* **342**, 373 (2013).
- [41] P. Blinder, A. Y. Shih, C. Rafie, and D. Kleinfeld, *Proc. Natl. Acad. Sci. USA* **107**, 12670 (2010).
- [42] M. Bertsch, B. Franchi, L. Meacci, M. Primicerio, and M. C. Tesi, *Euro. J. Appl. Math.* **32**, 749 (2021).
- [43] V. E. Johnson, W. Stewart, and D. H. Smith, *Nat. Rev. Neurosci.* **11**, 361 (2010).
- [44] S. Abu Hamdeh, E. R. Waara, C. Möller, L. Söderberg, I. Basun, H. Alafuzoff, L. Hillered, L. Lannfelt, M. Ingelsson, and N. Marklund, *Brain Pathol.* **28**, 451 (2018).
- [45] J. J. Iliff, M. J. Chen, B. A. Plog, D. M. Zeppenfeld, M. Soltero, L. Yang, I. Singh, R. Deane, and M. Nedergaard, *J. Neurosci.* **34**, 16180 (2014).
- [46] B. C. Reeves, J. K. Karimy, A. J. Kundishora, H. Mestre, H. M. Cerci, C. Matouk, S. L. Alper, I. Lundgaard, M. Nedergaard, and K. T. Kahle, *Trends Mol. Med.* **26**, 285 (2020).
- [47] B. T. Kress, J. J. Iliff, M. Xia, M. Wang, H. S. Wei, D. Zeppenfeld, L. Xie, H. Kang, J. A. Xu, Q. Liew *et al.*, *Ann. Neurol.* **76**, 845 (2014).
- [48] Q. Ma, B. V. Ineichen, M. Detmar, and S. T. Proulx, *Nat. Commun.* **8**, 1434 (2017).
- [49] S. Takeda, T. Hashimoto, A. D. Roe, Y. Hori, T. L. Spires-Jones, and B. T. Hyman, *FASEB J.* **27**, 3239 (2013).
- [50] H. Ding, P. T. Wong, E. L. Lee, A. Gafni, and D. G. Steel, *Biophys. J.* **97**, 912 (2009).
- [51] D. Watson, E. Castaño, T. A. Kokjohn, Y.-M. Kuo, Y. Lyubchenko, D. Pinsky, E. S. Connolly, C. Esh, D. C. Luehrs, W. B. Stine *et al.*, *Neurol. Res.* **27**, 869 (2005).
- [52] G. Meisl, C. K. Xu, J. D. Taylor, T. C. Michaels, A. Levin, D. Otzen, D. Klenerman, S. Matthews, S. Linse, M. Andreasen *et al.*, *Sci. Adv.* **8**, eabn6831 (2022).
- [53] L. Xue, L. Huangfu, R. Du, L. Chen, C. Yu, L. Xiong, and T. Wang, *Neurol. Res.* **44**, 1053 (2022).
- [54] L. J. Young, G. S. K. Schierle, and C. F. Kaminski, *Phys. Chem. Chem. Phys.* **19**, 27987 (2017).
- [55] F. Romanò, V. Suresh, P. Galie, and J. Grotberg, *Sci. Rep.* **10**, 21065 (2020).
- [56] R. Kedarasetti, P. Drew, and F. Costanzo, *Fluids Barriers CNS* **19**, 34 (2022).

- [57] H. E. Schreder, J. Liu, D. H. Kelley, J. H. Thomas, and K. A. Boster, *J. R. Soc. Interface* **19**, 20210812 (2022).
- [58] N. Korogod, C. C. H. Petersen, and G. W. Knott, *eLife* **4**, e05793 (2015).
- [59] H. Mestre, T. Du, A. M. Sweeney, G. Liu, A. J. Samson, W. Peng, K. N. Mortensen, F. F. Stæger, P. A. R. Bork, L. Bashford *et al.*, *Science* **367**, eaax7171 (2020).
- [60] A. J. Schain, A. Melo-Carrillo, A. M. Strassman, and R. Burstein, *J. Neurosci.* **37**, 2904 (2017).
- [61] T. Du, H. Mestre, B. T. Kress, G. Liu, A. M. Sweeney, A. J. Samson, M. K. Rasmussen, K. N. Mortensen, P. A. Bork, W. Peng *et al.*, *Brain* **145**, 787 (2022).
- [62] S. Mukherjee, M. Mirzaee, and J. Tithof, *Sci. Rep.* **13**, 12405 (2023).